Alexandria Engineering Journal (2016) xxx, xxx–xxx

HOSTED BY

Alexandria University

Alexandria Engineering Journal

www.elsevier.com/locate/aej
www.sciencedirect.com

ORIGINAL ARTICLE

Finite element simulation of magnetohydrodynamic convective nanofluid slip flow in porous media with nonlinear radiation

M.J. Uddin [a,*], Puneet Rana [b], O. Anwar Bég [c], A.I.Md. Ismail [d]

[a] American International University-Bangladesh, Bangladesh
[b] Department of Mathematics, Jaypee Institute of Information Technology, India
[c] Engineering Division, Room G77, Newton Building, School of Computing, Science and Engineering (CSE), University of Salford, M54WT, UK
[d] School of Mathematical Sciences, Universiti Sains Malaysia, Penang 11800, Malaysia

Received 24 January 2016; revised 27 February 2016; accepted 12 April 2016

KEYWORDS

Darcy porous medium;
Finite element;
MHD slip flow;
Nonlinear radiation;
Zero mass flux

Abstract A numerical investigation of two dimensional steady state laminar boundary layer flow of a viscous electrically-conducting nanofluid in the vicinity of a stretching/shrinking porous flat plate located in a Darcian porous medium is performed. The nonlinear Rosseland radiation effect is taken into account. Velocity slip and thermal slip at the boundary as well as the newly developed zero mass flux boundary conditions are also implemented to achieve physically applicable results. The governing transport equations are reduced to a system of nonlinear ordinary differential equations using appropriate similarity transformations and these are then solved numerically using a variational finite element method (**FEM**). The influence of the governing parameters (Darcy number, magnetic field, velocity and thermal slip, temperature ratio, transpiration, Brownian motion, thermophoresis, Lewis number and Reynolds number) on the dimensionless velocity, temperature, nanoparticle volume fraction as well as the skin friction, the heat transfer rates and the mass transfer rates are examined and illustrated in detail. The FEM code is validated with earlier studies for non-magnetic non-slip flow demonstrating close correlation. The present study is relevant to high-temperature nano-materials processing operations.

1. Introduction

A suspension of nanometer-sized particles/fibers in a base liquid changes the carrier fluid properties (viscosity, density, thermal conductivity, mass diffusivity) and is regarded as a "nanofluid". Water, organic liquids, kerosene, lubricants, bio-fluids, and polymeric solution are normally used as base fluids. Nanoparticles are made from various materials such

* Corresponding author.
E-mail address: jashim_74@yahoo.com (M.J. Uddin).
Peer review under responsibility of Faculty of Engineering, Alexandria University.

http://dx.doi.org/10.1016/j.aej.2016.04.021

Please cite this article in press as: M.J. Uddin et al., Finite element simulation of magnetohydrodynamic convective nanofluid slip flow in porous media with nonlinear radiation, Alexandria Eng. J. (2016), http://dx.doi.org/10.1016/j.aej.2016.04.021

Nomenclature

a	slip parameter (–)
b	thermal slip parameter (–)
B_0	constant magnetic field (telsa)
C	dimensional concentration
c_p	specific heat at constant pressure (J/kg K)
$C_{f\bar{x}}$	skin friction factor (–)
Da	Darcy number (–)
$Da_{\bar{x}}$	local Darcy number (–)
D_B	Brownian diffusion coefficient (m^2/s)
D_T	thermophoretic diffusion coefficient (m^2/s)
D_1	thermal slip factor (1/s)
$f(\eta)$	dimensionless stream function (–)
f_w	suction/injection parameter (–)
K_p	permeability of the porous medium (m^2)
k	thermal conductivity (m^2/s)
k_1	Rosseland mean absorption coefficient (1/m)
L	characteristic length of the plate (m)
Le	Lewis number (–)
M	magnetic field parameter (–)
$N_1(\bar{x})$	variable velocity slip factor (s/m)
Nb	Brownian motion parameter (–)
Nt	thermophoresis parameter (–)
$Nu_{\bar{x}}$	heat transfer rate
Pr	Prandtl number (–)
p	pressure (Pa)
q_m	wall mass flux ($kg/s\ m^2$)
q_w	wall heat flux (W/m^2)
R	conduction–radiation parameter (–)
Re	Reynolds number (–)
$Re_{\bar{x}}$	local Reynolds number (–)
$Sh_{\bar{x}}$	local Sherwood number (–)
T	dimensional temperature (K)
$\bar{u},\ \bar{v}$	velocity components along the axes (m/s)
$\bar{u}_w$	velocity of the plate (m/s)
$\bar{u}_e$	external velocity (m/s)
U_∞	reference velocity (m/s)
$\bar{x}, \bar{y}$	Cartesian coordinates aligned along and normal to the plate (m)

Greek symbols

α	thermal diffusivity (m^2/s)
α_i	real numbers (–)
β	pressure gradient parameter (–)
τ	ratio of effective heat capacity of the nanoparticle material to the heat capacity of the fluid (–)
σ	electric conductivity
σ_1	Stefan–Boltzmann constant
$\theta(\eta)$	dimensionless temperature (–)
θ_w	wall temperature excess ratio parameter (–)
$\phi(\eta)$	dimensionless concentration (nanoparticle volume fraction) (–)
η	similarity variable (–)
μ	dynamic viscosity of the fluid (Ns/m^2)
ν	kinematic viscosity of the fluid (m^2/s)
ρ_f	fluid density (kg/m^3)
ψ	stream function (–)

Subscripts

w	condition at the wall
∞	ambient condition

as oxide ceramics, metal nitride, carbide ceramics, metals and various forms of carbons [1]. Nanofluids have been proven to have diverse engineering and biomedical applications in both porous and purely fluid systems. Representative examples include the following: advanced nuclear systems, fuel cells and drug delivery. Micro-electro-mechanical systems (MEMS), nano-electro-mechanical systems (NEMS) and indeed many thermo-technical devices produce a huge amount of heat, which affects the normal activities of the devices and reduces the longevity. Hence, an efficient cooling (heating) system is required in designing such devices. It is known that heat transfer capacity of fluid can be improved by changing (i) flow geometry, (ii) boundary conditions, (iii) enhancing thermal conductivity, and (iv) using porous media [2]. Choi [3] has shown that nanoparticles can be used to enhance thermal conductivity of the base fluid. Transport phenomena associated with the flow of nanofluids have received the attention of investigators due to their diverse applications where heat and/or mass transfer play a vital role. The combination of a porous medium and nanofluid can significantly improve the effective heat transfer characteristics [4]. Therefore deployment of porous media in thermal engineering systems has been the subject of extensive activity in engineering sciences. Porous media arise in an astonishing range of technical and environmental applications including filtration, thermal insulation (fabrics and building materials), groundwater hydrology, oil reservoir formations, combustion, biomechanics, food stuffs and many types of heat exchanger [4]. In power station systems, cooling/heating is essential (e.g. in turbine blades), heat dissipation in electronic equipment and combustion systems (burners) to maintain efficient operation of the systems. The mixing of the low and high energy fluids which occur in these applications significantly affects the performance of these devices [5]. One of the ways to boost heat transfer (and cool boundaries) is to employ a porous medium saturated with nanofluid. Fundamental and detailed expositions of engineering applications of porous media such as solar energy collectors, heat exchangers, geothermics and heat pipes are documented in a number of monographs [6–9]. Nanofluids can and have been successfully utilized in many technologies, especially those that involve significant enhancement of heat transfer, and an excellent elaboration in this regard is Yu and Xie [10] (and references contained therein). For example, nanofluids can *increase the cooling rates* of heavy-duty engines by increasing the efficiency and reducing the complexity of thermal management systems and are a sustainable and relatively inexpensive mechanism for doing so [4]. So far, two popular mathematical formulations for nanofluid transport

Please cite this article in press as: M.J. Uddin et al., Finite element simulation of magnetohydrodynamic convective nanofluid slip flow in porous media with nonlinear radiation, Alexandria Eng. J. (2016), http://dx.doi.org/10.1016/j.aej.2016.04.021

phenomena have emerged, namely (i) Buongiorno's [11] model (wherein the Brownian motion and thermophoresis effects are prioritized) and (ii) the Tiwari–Das [12] model (which takes into account the solid volume fraction). Among these two models the Buongiorno [11] model is most frequently employed since it does not require actual nanofluid thermophysical properties, which are essential for the Tiwari–Das model [13]. However, Buongiorno's model generates a separate conservation equation for species diffusion (nano-particle volume concentration), whereas the Tiwari–Das model only requires balance equations for momentum and energy (heat) conservation. Overall however the Buongiorno's [11] model provides more detailed information on heat, mass and momentum characteristics. Many authors have extended this model to investigate various transport phenomena external (or internal) to various flow geometries subject to various initial and boundary conditions in porous/non-porous media. Examples in this regard include Nield and Kuznetsov [13], Chamkha et al. [14], Noghrehabadi and Behseresht [15] (for convection from a vertical plate in porous media), Rashad et al. [16] (for convection from a cone in Darcy porous media), Mahdy and Ahmed [17] (for vertical wavy surface convection), Cheng [18] (for a truncated cone), Behseresht et al. [19] (vertical cone in a non-Darcy porous medium), and Srinivasacharya and Surender [20] (for stratified porous media). Recent studies of nanofluid flow in porous media and their applications can be found in the review of Mahdi et al. [21] and the literature referenced therein.

Microscale and nanoscale heat/mass transfer have also stimulated the interest of engineers [22]. In microfluidics/nano-fluidics devices, the flow of a fluid on the micro/nanoscale differs significantly from the macroscopic flow. To incorporate the scaling effects of fluid flow at the submicron scale, the conventional *no-slip* boundary conditions at the fluid–solid interface must be replaced by *slip* (non-adherence) boundary conditions (velocity and thermal slip). The slip conditions display the interfacial interaction between a fluid and a solid, including contributions from surface roughness and intermolecular interaction [23]. Wen-Ming et al. [24] reported various slip models for gas microflow based on different theoretical, computational and experimental studies. Many analytical and numerical methods have been used to simulate a wide range of slip flows. Tripathi et al. [25] used homotopy semi-computational methods to study momentum slip effects on peristaltic propulsion of viscoelastic fluids. Nandeppanavar et al. [26] studied numerically the effect of first and second order slip on boundary layer flow past a stretching sheet. Bhargava et al. [27] used a finite element method to show that increasing wall slip factor strongly decelerates the radial and azimuthal flow in Von-Karman swirling convection. Khader and Megahed [28] studied the effect of second order slip and Eckert heating on Sakiadis flow in porous media using a Chebyshev finite difference method, and observing that slip velocity parameter decreases the skin-friction coefficient. Haq et al. [29] studied thermal radiation and slip effects on magnetohydrodynamic (MHD) stagnation point flow and showed that the local Nusselt number decreases with the momentum (velocity) slip parameter. Behzad et al. [22] investigate the temperature-dependent fluid properties and slip effect on microspherical particle. They found that a large slip on the wall increases convection along the surface while a large temperature jump reduces the heat transfer, emphasizing that neglecting temperature jump results in an *over-estimation* of the heat transfer rates. Nikbakhti and Rahimi [30] studied double-diffusive natural convection in a rectangular cavity with partially thermally active sides. Nikbakhti and Saberi [31] discussed natural convection heat and mass transfer in a rectangular porous cavity having partially thermally active walls.

It seems that most researchers have deployed conventional boundary conditions at the interface in boundary layer nanofluid simulations. However, no slip boundary conditions yield practically less applicable results [32]. Therefore to attain more realistic results, in this paper we investigate MHD flow from a nonlinearly radiating stretching sheet embedded in a porous medium, in the presence of the velocity slip, thermal slip and zero mass flux boundary conditions. The isotropic Darcy model is employed, valid for low-speed transport (viscous-dominated) and generally reliable up to Reynolds numbers of 10. This problem is of interest in nanomaterial manufacturing processes. The governing partial differential boundary layer equations are reduced to a two-point boundary value problem with the aid of appropriate similarity variables and solved with a finite element method (**FEM**). The effects of the thermophysical parameters on the fluid velocity, temperature and nanoparticle volume fraction (nanoparticle volume fraction), friction and heat transfer rates are examined in detail. Verification of computations with previous studies in the literature is also included.

2. Mathematical magnetic nanofluid slip transport model

The regime studied is a two-dimensional steady flow with a coordinate system in which the $\bar{x}$-axis is aligned vertically and the $\bar{y}$-axis is normal to it. A uniform transverse magnetic field of strength B_0 is imposed parallel to the $\bar{y}$-axis. The flow model and coordinate system are shown in Fig. 1. The magnetic Reynolds number is considered sufficiently small compared to applied magnetic field so as to ignore induced magnetic field effects. The electric field resulting from the polarization of charges and Hall effects is neglected. The fluid properties are assumed to be constant. Three distinct boundary layers (momentum, thermal and nanoparticle species) are formed in the vicinity of the plate. The boundary layer is optically thick and the Rosseland approximation for radiative heat transfer is valid [33]. Thus, the radiative heat flux for an optically thick boundary layer as described by Sparrow and Cess [34] is defined as $q_r = -\frac{4\sigma_1}{3k_1}\frac{\partial T^4}{\partial \bar{y}}$, where σ_1 ($= 5.67 \times 10^{-8}\,\mathrm{W/m^2\,K^4}$) is the Stefan–Boltzmann constant and k_1 ($\mathrm{m^{-1}}$) is the Rosseland mean absorption coefficient. The appropriate boundary layer equations are the conservation of mass, momentum, thermal energy and the nanoparticle volume fraction (species). These equations can be written in dimensional form by extending the formulations of Buongiorno [11] and Makinde and Aziz [35] as follows:

$$\frac{\partial \bar{u}}{\partial \bar{x}} + \frac{\partial \bar{v}}{\partial \bar{y}} = 0, \tag{1}$$

$$\rho_f\left(\bar{u}\frac{\partial \bar{u}}{\partial \bar{x}} + \bar{v}\frac{\partial \bar{u}}{\partial \bar{y}}\right) = K\rho_f \bar{u}_e \frac{d\bar{u}_e}{d\bar{x}} + \mu\frac{\partial^2 \bar{u}}{\partial \bar{y}^2} - \frac{\mu}{K_P}(\bar{u} - K\bar{u}_e) - \sigma B_0^2(\bar{u} - K\bar{u}_e), \tag{2}$$

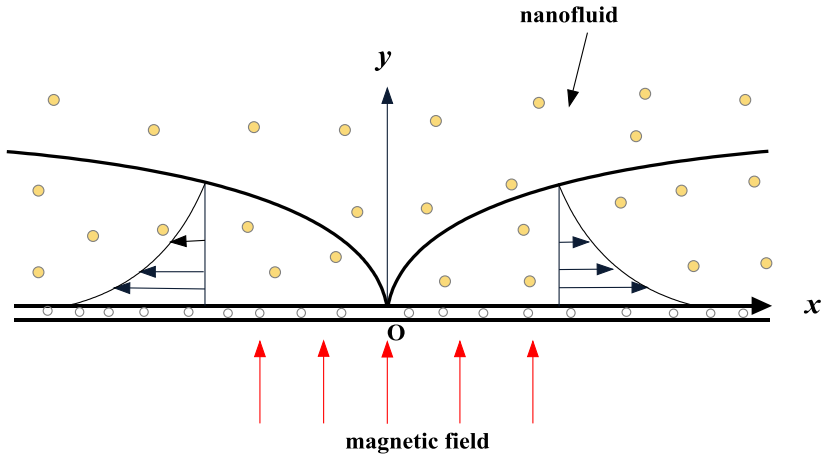

(a) permeable stretching sheet (λ>0)

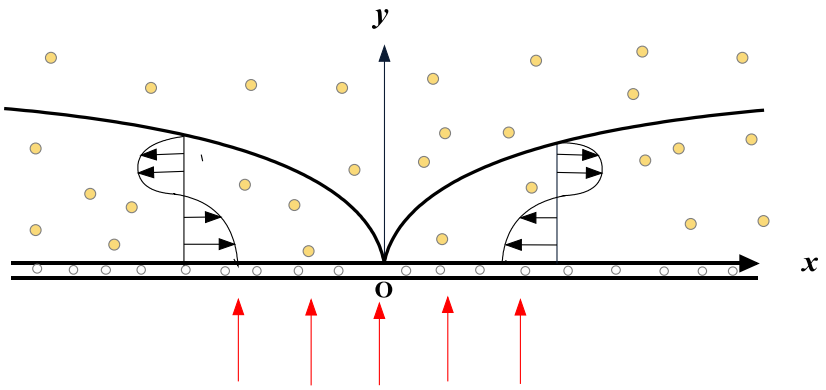

(b) permeable shrinking sheet (λ<0)

Figure 1 Physical model and coordinates system.

$$\bar{u}\frac{\partial T}{\partial \bar{x}}+\bar{v}\frac{\partial T}{\partial \bar{y}}=\alpha\frac{\partial^2 T}{\partial \bar{y}^2}+\tau\left\{D_B\frac{\partial C}{\partial \bar{y}}\frac{\partial T}{\partial \bar{y}}+\left(\frac{D_T}{T_\infty}\right)\left(\frac{\partial T}{\partial \bar{y}}\right)^2\right\}-\frac{1}{\rho_f c_p}\frac{\partial q_r}{\partial \bar{y}}, \tag{3}$$

$$\bar{u}\frac{\partial C}{\partial \bar{x}}+\bar{v}\frac{\partial C}{\partial \bar{y}}=D_B\frac{\partial^2 C}{\partial \bar{y}^2}+\left(\frac{D_T}{T_\infty}\right)\frac{\partial^2 T}{\partial \bar{y}^2}. \tag{4}$$

The appropriate boundary conditions are [32,36]:

$$\bar{u}=\lambda\bar{u}_w+\bar{u}_{\text{slip}},\ \bar{v}=v_w,\ T=T_w+T_{\text{slip}},\ D_B\frac{\partial C}{\partial \bar{y}}+\frac{D_T}{T_\infty}\frac{\partial T}{\partial \bar{y}}=0\ \text{at}\ \bar{y}=0,$$
$$\bar{u}\to K_p\bar{u}_e,\ T\to T_\infty,\ C\to C_\infty\ \text{as}\ \bar{y}\to\infty. \tag{5}$$

Here the following notation applies: $\alpha=\frac{k}{(\rho c)_f}$: thermal diffusivity of the fluid, $\tau=\frac{(\rho c)_p}{(\rho c)_f}$: ratio of heat capacity of the nanoparticle and fluid, K_p: permeability of the medium, $(\bar{u},\bar{v})$: velocity components along $\bar{x}$ and $\bar{y}$ axes, $\bar{u}_w=\frac{U_r\bar{x}}{L}$: velocity of the plate, $\bar{u}_e=\frac{U_r\bar{x}}{L}$: free stream velocity of the plate, L: characteristic length of the plate, $\bar{u}_{\text{slip}}=N_1\,v\,\frac{\partial \bar{u}}{\partial \bar{y}}$: linear slip velocity, N_1: velocity slip factor, $T_{\text{slip}}=D_1\frac{\partial T}{\partial \bar{y}}$: thermal slip, D_1: thermal slip factor, ρ_f: density of the base fluid, μ: dynamic viscosity of the base fluid, ρ_p: density of the nanoparticles, $(\rho C_P)_f$: heat effective heat capacity of the fluid, $(\rho C_P)_p$: effective heat capacity of the nanoparticle material, D_B: Brownian diffusion coefficient, D_T: thermophoretic diffusion coefficient. $K=0$ corresponds to the case without the pressure gradient term and $K=1$ implies flow with a pressure gradient term present, $\bar{u}_w$: velocity of the sheet, $\lambda>0$ represents a *stretching* sheet, while $\lambda<0$ represents a *shrinking* sheet, and $\lambda=0$ represents a static sheet (stationary wall scenario). Before solving the physical problem described by the set of Eqs. (1)–(5), it is pertinent to perform a transformation of variables. We introduce therefore the following similarity variables [31]:

$$\eta=\frac{\bar{y}}{\sqrt{K_p}},\ \psi=U_r\frac{\bar{x}}{L}\sqrt{K_p}f(\eta),\ \theta(\eta)=\frac{T-T_\infty}{T_w-T_\infty},\ \phi(\eta)=\frac{C-C_\infty}{C_\infty}. \tag{6}$$

These expressions satisfy Eq. (1) identically and substitution of these into Eqs. (2)–(5) yields the following:

$$f'''+(K-f')+Re\,Da\left[ff''-f'^2+K+M^2(K-f')\right]=0, \tag{7}$$

$$\theta'' + Re\,Pr\,Daf\theta' + Pr[Nb\,\theta'\,\phi' + Nt\,\theta'^2]' + \frac{4}{3R}[\{1+(T_r-1)\theta\}^3\theta']' = 0, \quad (8)$$

$$\phi'' + Le\,Re\,Daf\phi' + \frac{Nt}{Nb}\theta'' = 0. \quad (9)$$

The boundary conditions in Eq. (5) become the following:

$$f(0) = fw,\ f'(0) = \lambda + af''(0),\ \theta(0) = 1 + b\,\theta'(0),\ Nb\,\phi'(0) + Nt\,\theta'(0) = 0,\ f'(\infty) = K,\ \theta(\infty) = \phi(\infty) = 0. \quad (10)$$

In Eqs. (7)–(10) primes denote *ordinary* differentiation with respect to η. The thermophysical dimensionless parameters arising in Eqs. (7)–(10) are defined as follows: $Re = \frac{U_r L}{\nu}$ is Reynolds number, $Da = \frac{K_p}{L^2}$ is Darcy number, $Pr = \frac{\nu}{\alpha}$ is the Prandtl number, $Nt = \frac{\tau D_T (T_w - T_\infty)}{\nu T_\infty}$ is the thermophoresis parameter, $Nb = \frac{\tau D_B C_\infty}{\nu}$ is the Brownian motion parameter, $Le = \frac{\nu}{D_B}$ is the Lewis number, $a = \frac{N_1 \nu}{\sqrt{K_P}}$ is the hydrodynamic slip parameter, $b = \frac{D_1}{\sqrt{K_P}}$ is the thermal slip parameter, $f_w = \frac{v_w L}{U_r \sqrt{K_p}}$ is the suction/injection parameter, $\theta_w = \frac{T_w}{T_\infty}$ is wall temperature excess ratio parameter, $R = \frac{k k_1}{4\sigma_1 T_\infty^3}$ is conduction–radiation parameter and $M^2 = \frac{\sigma B_0^2 L}{U_r \rho}$ is the magnetic field parameter (ratio of magnetic body force to inertial hydrodynamic force).

To estimate the performance of the various microfluidic/-nanofluid as well as thermal devices, the knowledge of drag and heat transfer rates at the wall is important. The information associated with wall property variation yields information which may lead to an improvement in the design of the devices for increased performance and efficiency [37]. Thus the skin friction, heat transfer and mass transfer rates are the important quantities that need to be quantified. Following Uddin et al. [33], these quantities of can be written in the following form:

$$C_{f\bar{x}} Re_{\bar{x}}^{-1} Da_{\bar{x}}^{0.5} = 2f''(0),\ Nur = Nu_{\bar{x}} Da_{\bar{x}}^{0.5} = -\left[1 + \frac{4}{3R}\{1+(T_r-1)\theta(0)\}^3\right]\theta'(0),\ Shr = Sh_{\bar{x}} Da_{\bar{x}}^{0.5} = -\frac{\phi'(0)}{\phi(0)}, \quad (11)$$

where $Da_{\bar{x}} = \frac{K_p}{\bar{x}^2}$ is the local Darcy number and $Re_{\bar{x}} = \frac{\bar{u}_w \bar{x}}{\nu}$ is the local Reynolds number.

3. Numerical solution with finite element method (FEM)

This section is devoted to the computational solution of Eqs. (7)–(10) to show the effect of the emerging parameters on the flow, heat and nanoparticle volume fraction characteristics. The purely analytical solution of Eqs. (7)–(10) is extremely difficult if not intractable. Hence a numerical approach is elected, specifically the finite element method (**FEM**) which is the most popular and adaptive method available for solving differential equations. FEM is exclusively employed in commercial softwares e.g. ANSYS, ADINA, MARC, ABAQUS. It very effectively solves boundary value problems very quickly and accurately. Although other approaches do exist which have been employed in nanofluid transport phenomena, e.g. Lattice Boltzmann Method (LBM), this is a particle-based approach and is popular in simulations involving powders, and more recently nano-particles. However it is primarily used by physicists for polymeric suspension, liquid crystal simulations, etc., not engineers, who prefer (justifiably) the finite element method which is much simpler and just as accurate. The authors are aware of this method but have elected FEM as we are examining boundary layer phenomena with nano-scale effects, not considering particle–particle interactions, for which LBM was originally developed. LBM simulates fluids in the molecular state rather than at the classical macroscopic level and involves solving the Boltzmann transport equation for particle distribution functions on a simplified phase space, designated the lattice. Other variations of LBM for heat transfer of relevance to nanofluids are the thermal LBM which models the dynamics of fluid particles to capture macroscopic fluid quantities such as velocity, pressure and temperature. In this approach, the fluid domain is discretized to uniform Cartesian cells. The probability of finding particles within a certain range of velocities at a certain range of locations replaces tagging each particle as in the computationally-intensive molecular dynamic simulation approach. In LBM, each cell holds a fixed number of distribution functions, which represent the number of fluid particles moving in these discrete directions. Popular models are the D2Q9 model. The main advantage of LBM over FEM (and for example other computational fluid dynamic methods such as the finite volume method, FVM, which is used in e.g. ANSYS-FLUENT) is that it can be easily parallelized and computationally less costly. However in the engineering community, most researchers use the Navier–Stokes viscous flow equations as the standard for laminar flow (from which boundary-layer theory is developed), and are therefore not acquainted with the Boltzmann model. LBM therefore while having its merits is less popular since it requires a higher knowledge of physics and gas dynamics and is not integratable generally into standard numerical methods used in engineering. Very few engineers in the experience of the authors have embraced LBM. Despite its advantages in terms of dissipation errors over Navier–Stokes type methods e.g. FEM, LBM is mathematically more complex and therefore not attractive to engineers. The basic concept of FEM is that the whole domain ("infinite") for the problem in any dimension is divided into smaller "finite elements". It is an extremely versatile (in terms of both resolving complex geometrical and material nonlinearity) and has received considerable attention in nonlinear nanofluid mechanics [38], heat transfer [39,40], membrane structural mechanics [41], electrical systems [42], biological systems [43], acoustics [44] and many other fields [45]. The steps involved in finite element analysis are as follows:

(i) Discretization of entire domain (boundary layer) into finite elements or pieces.
(ii) The generation of system of element equations.
(iii) Using connectivity matrix, the assembly of element equations for the whole domain.
(iv) Implementation of boundary conditions.
(v) Solution of final system of assembled equations.

The assembled equations obtained can be solved using any standard matrix technique such as Householder's method, Gauss's elimination method, LU Decomposition method and Choleski decomposition method. An issue is that of the shape

functions used to approximate actual functions. The "*weak form*" associated with Eqs. (7)–(9) over a typical linear element $\Omega_e = (\eta_e, \eta_{e+1})$, is given by the following:

$$\int_{\Omega_e} \{w_1(f' - h)\} = 0, \tag{12}$$

$$\int_{\Omega_e} \{w_2(h'' + (K - h) + Re\,Da[fh' - h^2 + K + M^2(K - h)])\} = 0, \tag{13}$$

$$\int_{\Omega_e} \left\{ w_3\left(\theta'' + Re\,Pr\,Daf\theta' + Pr\left[Nb\,\theta'\,\phi' + Nt\,\theta'^2\right]' + \frac{4}{3R}[\{1 + (T_r - 1)\theta\}^3\theta']' = 0,\right)\right\} = 0, \tag{14}$$

$$\int_{\Omega_e} \left\{ w_4\left(\phi'' + Le\,ReDaf\phi' + \frac{Nt}{Nb}\,\theta'' = 0\right)\right\} = 0, \tag{15}$$

where w_1, w_2, w_3 and w_4 are arbitrary test functions and may be viewed as the variation in f, h, g and θ, respectively. The finite element model can be obtained from the equations aforesaid by substituting in finite element approximations of the form:

$$f = \sum_{j=1}^{N} f_j\psi_j, \quad h = \sum_{j=1}^{N} h_j\psi_j, \quad \theta = \sum_{j=1}^{N} \theta_j\psi_j, \quad \phi = \sum_{j=1}^{N} \phi_j\psi_j, \tag{16}$$

where $N = 2$ (linear) or 3 (quadratic) with $w_1 = w_2 = w_3 = w_4 = \psi_i$, and for our computations, the shape functions of a typical element $\Omega_e = (\eta_e, \eta_{e+1})$ are as follows:

Linear element:

$$\psi_1^e = \frac{(\eta_{e+1} - \eta)}{(\eta_{e+1} - \eta_e)}, \quad \psi_2^e = \frac{(\eta - \eta_e)}{(\eta_{e+1} - \eta_e)}, \quad \eta_e \leqslant \eta \leqslant \eta_{e+1}. \tag{17}$$

Quadratic element:

$$\psi_1^e = \frac{(\eta_{e+1} - \eta_e - 2\eta)(\eta_{e+1} - \eta)}{(\eta_{e+1} - \eta_e)^2} \quad \psi_2^e = \frac{4(\eta - \eta_e)(\eta_{e+1} - \eta)}{(\eta_{e+1} - \eta_e)^2},$$
$$\psi_3^e = -\frac{(\eta_{e+1} - \eta_e - 2\eta)(\eta - \eta_e)}{(\eta_{e+1} - \eta_e)^2}, \ \eta_e \leqslant \eta \leqslant \eta_{e+1}. \tag{18}$$

The finite element model of is given by;

$$\begin{bmatrix} [K^{11}] & [K^{12}] & [K^{13}] & [K^{14}] \\ [K^{21}] & [K^{22}] & [K^{23}] & [K^{24}] \\ [K^{31}] & [K^{32}] & [K^{33}] & [K^{34}] \\ [K^{41}] & [K^{42}] & [K^{43}] & [K^{44}] \end{bmatrix} \begin{bmatrix} f \\ h \\ \theta \\ \phi \end{bmatrix} = \begin{bmatrix} \{b^1\} \\ \{b^2\} \\ \{b^3\} \\ \{b^4\} \end{bmatrix}, \tag{19}$$

where $[K^{mn}]$ and $[b^m]$ $(m, n = 1, 2, 3, 4)$. Each element matrix (order 8×8) is assembled after linearizing the system of equations and Gaussian quadrature is employed for solving the integrations. After applying the given boundary conditions, the final system of equations (**AX** = **b**) is solved using the Gauss elimination method and the entire algorithm has been executed in **MATLAB**. In the present computations, the boundary layer domain has been discretized to satisfy far-field boundary conditions η_∞ (at infinity) to ensure the asymptotic behavior of dependent variables. In the absence ($K = 0$) and presence of pressure gradient ($K = 1$), η_∞ is fixed at 30 and 10 respectively. An iterative process is assumed to attain a convergent solution when the following condition is satisfied:

$$\sum_i |\Theta_i^n - \Theta_i^{n-1}| \leqslant 10^{-6}. \tag{20}$$

The present problem reduces to Yih [46] when $a = b = Nt = 0$, $Re = Da = K = 1, Nb \to 0$ in Eqs. (7)–(10) and $\lambda = 0$, $Pr = \Omega = 1$ are prescribed in Yih paper [46]. Experimental data for the present model are not available in the literature. Hence, we compare our results with the published results to determine the accuracy of our results. The values of $-\theta'(0)$ are compared with Yih [46] in Table 1 and with Dayyan et al. [47] (NS = numerical solution, HAM = homotopy analysis method solution in this reference) in Table 2. Also the values of $-\theta'(0)$, $-\phi'(0)$ are compared with Khan and Pop [63] in Table 3. In each case, very good correlation has been achieved.

4. Computations and discussion

Fig. 2(a and b) shows the effects of the Reynolds number and the velocity slip parameter and the pressure gradient parameter K on the dimensionless velocity within the boundary layer. It is evident from Fig. 2(a) that the dimensionless velocity is decreased as the Reynolds number increases for both in the presence and in the absence of the slip parameter. A similar trend for velocity has been observed by Dayyan et al. [47] for non-magnetic pure fluid. The velocity slip parameter leads to reduction in the velocity i.e. deceleration. This figure is drawn when the pressure gradient term is absent. A reverse trend of the velocity is noticed when the pressure gradient term is present (when there is external velocity). A similar pattern in velocity response has been reported by Suhil and Al-Nimr [48], Jawad and Oubarra [49] for non-magnetic regular fluid (without nanofluid effects). The variations of the physical quantities with various parameters are shown in Tables 4 and 5 respectively.

Fig. 3(a and b) displays the effects of the Reynolds number and the velocity slip parameter on the dimensionless temperature within the thermal boundary layer. Fig. 3(a) indicates that the dimensionless velocity is decreased as the Reynolds number increases both in the presence and in the absence of the slip parameter. A similar trend for temperature was also noticed by Dayyan et al. [47] for non-magnetic pure fluid. In the presence of the pressure gradient term, a velocity slip reduces the temperature (Fig. 3(b)) i.e. cools the boundary layer. The suppression of temperature has also been computed by other researchers, notably Suhil and Al-Nimr [48] and Jawad and Oubarra [49] although for non-magnetic regular fluids. Note that the effect of the velocity slip is more visible for the flow field in the absence of the pressure gradient.

Table 1 Comparison of heat transfer rates at the surface $-\theta'(0)$ with Yih [46] (for $\Omega = 1$) as a special case keeping $Pr = K = Re = \theta_w = Da = 1$, $Nb = Nt = 10^{-6}$, $a = b = f_w = \lambda = 0$, $R \to \infty$.

M	Yih [46]	FEM – present results
0	0.595346	0.595346
0.5	–	0.600057
1.0	–	0.611991

Table 2 Validation of heat transfer rate at the surface $-\theta'(0)$ for different values of f_w, Pr and Re.

			Dayyan et al. [47]		FEM
f_w	Re	Pr	HAM	NS	Present results
0	1		0.5030	0.5033	0.501251
	1.5		0.6456	0.6422	0.641842
	2	1	0.7518	0.7592	0.759113
	5		1.2636	1.2576	1.257601
−0.3		0.5	0.216	0.219	0.188511
	1	1	0.3128	0.313	0.306187
		5	0.636	0.623	0.623307
0.3		0.5	0.4145	0.4100	0.399898
	1	1	0.7258	0.7216	0.721167
		5	2.5821	2.5826	2.582625

Table 3 Comparison of the rate of heat transfer at the surface $-\theta'(0)$ and $-\phi'(0)$ for different values of Nt and Nb with fixed nanoparticle nanoparticle volume fraction on the sheet, when $Pr = 10 = Le$, $a = b = K = M = f_w = 0$, $Re = \theta_w = Da = \lambda = 1$, $R \to \infty$.

		$-\theta'(0)$		$-\phi'(0)$	
Nt	Nb	Khan and Pop [63]	Present results	Khan and Pop [63]	FEM – present results
0.1	0.1	0.9524	0.952376	2.1294	2.129388
	0.3	0.2522	0.252155	2.4100	2.410015
	0.5	0.0543	0.054253	2.3836	2.383567
0.3	0.1	0.5201	0.520079	2.5286	2.528625
	0.3	0.1355	0.135514	2.6088	2.608812
	0.5	0.0291	0.029135	2.4984	2.498367
0.5	0.1	0.3211	0.321054	3.0351	3.035120
	0.3	0.0833	0.083298	2.7519	2.751866
	0.5	0.0179	0.017922	2.5731	2.573099

Fig. 4(a and b) depicts the effects of the Reynolds number and the velocity slip parameter on the dimensionless nanoparticle volume fraction. The dimensionless nanoparticle volume fraction is decreased as the Reynolds number increases in both

Table 4 Numerical values of skin friction coefficient $f''(0)$ and rate of the heat transfer at the surface $-\theta'(0)$ (in parenthesis) for different values of M, Re, a, b and λ when $Pr = 6.8$, $Le = 10$, $R = 1$, $\theta_w = 1.5$, $f_w = 0$, $Da = 0.1$, $Nb = Nt = 0.5$, $K = 1.0$.

			λ		
M	Re	(a, b)	−0.5	0	0.5
	1.5	(0.1, 0.1)	1.486481	1.015871	0.519908
			(0.181590)	(0.199662)	(0.218997)
0.5		(0.1, 0.2)	1.486481	1.015871	0.519908
			(0.180167)	(0.198089)	(0.217235)
		(0.2, 0.1)	1.360981	0.925897	0.471847
			(0.186289)	(0.203187)	(0.220847)
		(0.2, 0.2)	1.360981	0.925897	0.471847
			(0.184830)	(0.201582)	(0.219066)
	1.5		1.547557	1.055186	0.538924
			(0.183453)	(0.200924)	(0.219608)
1.0	3.0	(0.1, 0.1)	1.708311	1.179385	0.608817
			(0.246997)	(0.275731)	(0.306078)
	5.0		1.897106	1.322127	0.687645
			(0.309807)	(0.349972)	(0.391756)
0			1.429819	0.987028	0.509182
			(0.246364)	(0.274885)	(0.303934)
0.5	3.0	(0.2, 0.2)	1.461287	1.006606	0.518376
			(0.248089)	(0.275988)	(0.304441)
1.0			1.549120	1.061599	0.544337
			(0.252719)	(0.278967)	(0.305825)

the presence and the absence of the velocity slip and both in the presence and in the absence of the pressure gradient term. This correlates well with Dayyan et al. [47] for non-magnetic pure fluid. The velocity slip parameter leads to an increase in the nanoparticle volume fraction. Note that the temperature is not affected by the pressure gradient term as the momentum equation is not coupled with the thermal equation. It is therefore evident that velocity slip encourages diffusion of the nanoparticles into the boundary layer and generates more homogenous concentration levels. This elevates the concentration boundary layer thickness. Slip at the wall can therefore be judiciously utilized to alter the structure of nano-materials in stretching/shrinking sheets, an important characteristic in material processing.

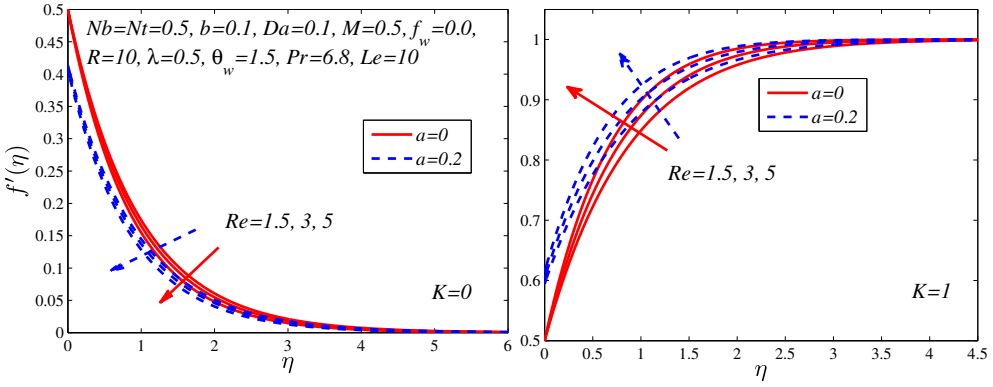

Figure 2 (a and b) Effect of the Reynolds number and the velocity slip parameter on dimensionless velocity.

Table 5 Numerical values of local rate of the heat transfer at the surface $-\theta'(0)$ for different values of K, R, Nt and f_w keeping $Pr = 6.8$, $Le = 10$, $\lambda = Nb = M = 0.5$, $a = b = 0.1$, $\theta_w = 1.5$, $Da = 0.1$, $Re = 3.0$.

			f_w		
K	R	Nt	−0.3	0.0	0.3
0	→∞	0.1	0.133517	0.450359	0.804159
		0.3	0.146167	0.355352	0.609795
		0.5	0.217202	0.278179	0.465986
	10	0.1	0.059284	0.190066	0.327590
		0.3	0.052420	0.161179	0.274658
		0.5	0.046256	0.137665	0.232773
1	→∞	0.1	0.599064	0.830769	0.557015
		0.3	0.628785	0.723758	0.489395
		0.5	0.670122	0.619978	0.431310
	10	0.1	0.370033	0.456826	0.557015
		0.3	0.356136	0.413422	0.489395
		0.5	0.340759	0.373402	0.431311

Fig. 5(a and b) depicts the effects of thermophoresis and conduction–radiation parameters on the dimensionless temperature. Dimensionless temperature is increased as the thermophoresis parameter increases for both radiating and non-radiating sheets, both in the presence and in the absence of the pressure gradient term. In the absence of the pressure gradient term, temperature is decreased as the radiation parameter increases. A similar trend of temperature was also observed by Hossain et al. [50] and Uddin et al. [33] which yields a further verification of the FEM numerical computations. The parameter, is conduction–radiation parameter, $R = \frac{k k_1}{4\sigma_1 T_\infty^3}$ arises in the augmented heat conduction term in Eq. (8), via the fraction $4/3R$. Greater values of R imply weaker radiative heat transfer contribution and vice versa for smaller values. When $R = 1$ both thermal conduction and thermal radiation contribute equally to the temperature field and when $R \to \infty$ radiative effects vanish. Inspection of Fig. 5(a and b) shows that temperatures are always higher for $R = 10$ than for $R \to \infty$. This is consistent with the high temperatures experienced with radiation (the Stefan–Boltzmann law is fourth order in temperature) and demonstrates that radiation achieves significantly greater heating of the nanofluid than conduction or convection. This is attributable to the propagation of electromagnetic waves in radiation which are absent in other modes of heat transfer. Even with a relatively simple model such as Rosseland's diffusive flux model, the effect is substantial. We further note that the current radiative model is valid for high optical thickness (optical depth) for which thermal radiation is better attenuated in the medium and is known to induce heating, as elaborated by Lord and Arpaci [51] who have computed significant rise in temperatures with increasing optical thickness. Of course the present simulations may be refined to consider more complex models e.g. Schuster–Schwartzchild two-flux models, discrete ordinate models, and these are under consideration. Effectively

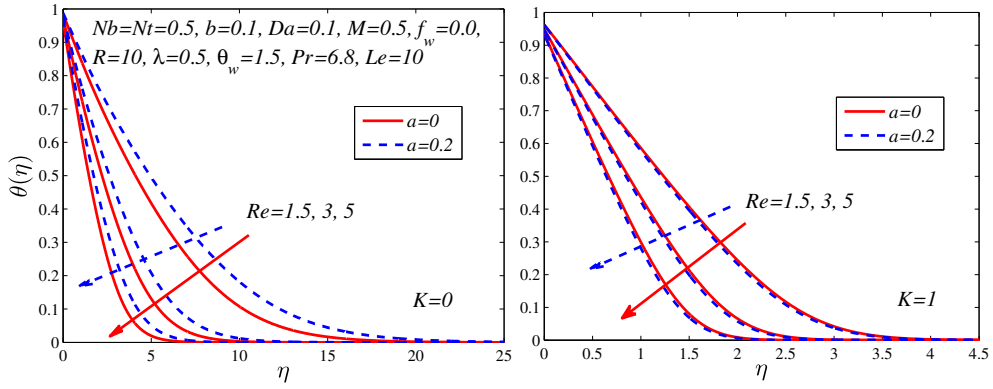

Figure 3 (a and b) Effect of the Reynolds number and velocity slip parameter on dimensionless temperature.

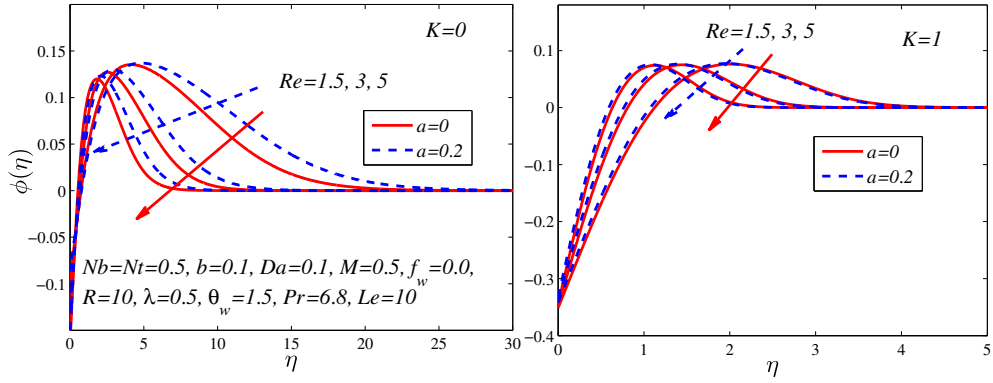

Figure 4 (a and b) Effect of Reynolds number and velocity slip parameter on dimensionless concentration.

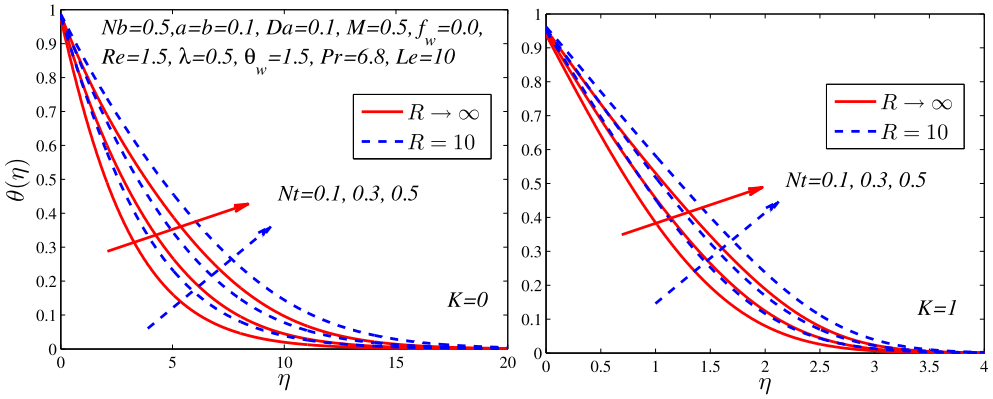

Figure 5 (a and b) Effect of thermophoresis and radiation parameter on dimensionless temperature.

the present computations show that thermal boundary layer thickness of nanofluid will be enhanced with greater radiative effects (smaller R values).

Fig. 6(a and b) depicts the effects of thermophoresis and the conduction–radiation parameters on the dimensionless nanoparticle volume fraction, with ($K = 1$) and without ($K = 0$) pressure gradient. The dimensionless nanoparticle volume fraction is increased as the thermophoresis parameter increases for both radiating ($R = 10$) and non-radiating ($R \to \infty$) sheet flows both in the presence and in the absence of the pressure gradient term. Particle thermophoresis is known to be a non-equilibrium cross-flow effect between mass and heat transport and resembles to some extent thermo-diffusion (the Soret effect) in simple fluid mixtures. In nanofluids and other suspensions of particles, particle drift is induced by the force of a temperature gradient. Numerous studies have shown e.g. Buongiorno [11] and more recently Pakravan and Yaghoubi [52], that within nanofluids subjected to a temperature gradient, dispersed particles exhibit in addition to Brownian motion, a steady drift velocity which is a function of the thermophoresis coefficient (D_T). Depending on the sign of D_T, the nanoparticles focus either at the cold or at the hot side, giving rise to the steady-state concentration gradient. In the present analysis, the sign is positive (see Eqs. (8) and (9)). The thermophoretic effect is similar to the behavior of particles subjected to an external driving force (e.g. gravity, electric field), however in thermophoresis there is *no real external field* present. The present computations confirm that nanoparticles migrate away from the sheet wall toward the boundary layer regime, which is heated via thermophoresis and this effect simultaneously assists particle deposition in the body of nanofluid, thereby accounting for the elevated concentration (nanoparticle) magnitudes. In the absence of the pressure gradient term, nanoparticle volume fraction is enhanced as the radiation parameter increases. Species diffusion is therefore assisted with radiative flux. Recently, a similar trend of temperature was observed by Uddin et al. [33] using **MAPLE** numerical quadrature. Other researchers e.g. Hady et al. [53] and Sheikholeslami et al. [54] have also reported a significant elevation in nanofluid concentration boundary layer thickness with greater thermal radiation effect.

Fig. 7(a and b) illustrates the influence of Darcy number and wall transpiration (suction/injection) parameter on dimensionless velocity distributions. The velocity is decreased (increased) as the Darcy number increases in the absence (presence) of the pressure gradient term for both plates with injection ($fw = -0.1$) and for both plates with suction ($fw = 0.1$). The Darcy model relates porous transport velocity to the pressure drop in the porous medium [55]. In the absence of such pressure gradient the flow is decelerated with greater permeability effect, contrary to correct response which is observed when pressure gradient is present ($K = 1$). In the present study we consider significantly porous media i.e. very large permeabilities and Darcy number is assigned relatively high values (0.1, 0.3, 0.5). These correspond to foam-based porous materials or sparsely-packed media through which the nanofluid

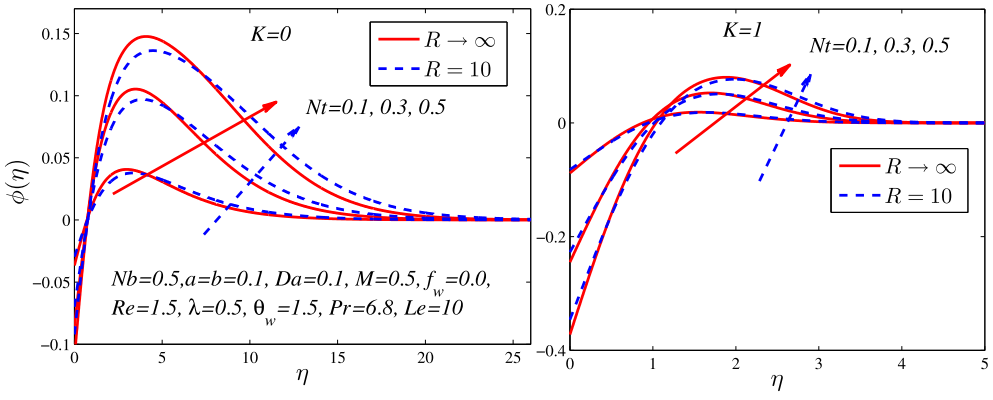

Figure 6 (a and b) Effect of thermophoresis and radiation parameter on dimensionless concentration.

sheet can be stretched or contracted. It is interesting to observe the significant deviation in profiles for the two cases in Fig. 7(a and b). Without pressure gradient, velocity decays from the sheet to vanish in the free stream of the boundary layer; however with pressure gradient present, the velocity field grows from the wall (sheet) to attain a maximum in the free stream. The scenario with pressure gradient is therefore more realistic since boundary layers attain highest values furthest from the boundary. The decreasing porous matrix resistance (Fig. 7 (b)) with greater Darcy number manifests in *decreased resistance* to the percolating nanofluid which results in *flow acceleration*. With injection, the flow is further accelerated and with suction it is retarded. Porous media therefore achieve an attractive control mechanism in boundary layer flows and this is of benefit in material processing.

Fig. 8(a and b) illustrates the effects of the Darcy number and suction/injection parameter on the dimensionless temperature. Temperature is decreased (increased) as the Darcy number increases in the absence (presence) of the pressure gradient term for both the case of wall injection ($fw = -0.1$) and wall suction ($fw = 0.1$). The progressively greater sparsity of packing in the porous medium with increasing permeability manifests in a decrease in solid fibers available for thermal conduction. This, despite the presence of thermal radiation ($R = 10$) results in a decrease in heat conduction which causes the drop in temperatures. Both with and without pressure gradient the mature of this response is similar, and distinct from the disparity in velocity distributions observed in Fig. 6(a and b). In both Fig. 8(a and b) the temperatures exhibit a monotonic decay from the wall to the free stream, a classical feature of thermal boundary layers, whether nanoscale or not. However in the presence of pressure gradient ($K = 1$), this plummet is more dramatic and the profiles reach vanishing values faster than in the absence of pressure gradient ($K = 0$). Strong blowing (injection) achieves a heating effect in the regime, whereas strong injection induces cooling. The thickening in the momentum boundary layer with suction (i.e. deceleration in the flow) is intimately connected to the thermal diffusion within it. Suction depletes thermal boundary layer thickness also. Evidently the combination of wall mass flux (suction/injection) with a porous medium exerts substantial influence on boundary layer characteristics for nanofluids.

Fig. 9(a and b) illustrates the effects of the Darcy number and suction/injection parameter on the dimensionless nanoparticle volume fraction. Initially in close proximity to the sheet, the nanoparticle volume fraction (species concentration) is decreased as the Darcy number increases in the absence and presence of the pressure gradient term for both injection ($fw = -0.1$) and suction ($fw = 0.1$). However further from the wall the response is reversed and it is found that the peak nanoparticle concentration arises at $\eta \approx 5$ with $Da = 0.5$ (maximum permeability). The diffusion of nano-particles (or indeed any species) in porous media is different from heat or fluid flow. The size of nano-particles influences the facility with which they can percolate via pore space, as elucidated by Vafai and Tien [56]. Even though the present porous structure is very high permeability, near the wall the packing of solid fibers will have a suppressing effect on nano-particle motion. This effect remains whether the medium is tortuous or not. This boundary effect usually requires a more sophisticated porous medium hydrodynamic model, and in this regard exponentially decaying porosity models have been developed, notably Vafai [57]. Evidently however the dominant effect of increasing Darcy number for the majority of the boundary layer regime transverse to the wall is to encourage mass transfer of nanoparticles, and again this trend has been identified for regular and complex suspension fluids in many studies, including Gebhart [58]. Generally blowing at the wall is found to enhance nano-particle diffusion and thicken the concentration boundary layer when pressure gradient is absent whereas the converse effect is largely prevalent in the presence of pressure gradient.

Fig. 10(a and b) displays the effects of the temperature ratio and the thermal slip parameter on the dimensionless temperature. The temperature is increased as the temperature ratio increases both in the absence and in the presence of the pressure gradient term for both the isothermal sheet scenario ($b = 0$) and the thermal slip sheet scenario ($b = 0.2$). We note that for both cases, temperature is reduced as the thermal slip parameter increases. This is due to the fact that with thermal slip present, the nanofluid in the neighborhood of the plate does not sense the heating effects of the plate and a decreasing quantity of heat is transferred from the hot sheet surface to the surrounding nanofluid. Although the nature of profiles for both pressure gradient presence and absence at first appears almost identical, closer inspection of the graphs reveals that with pressure gradient the temperatures descend much faster to the free stream vanishing value. Pressure gradient therefore results in a less homogenous distribution of temperature across the boundary layer compared with the case where it is absent.

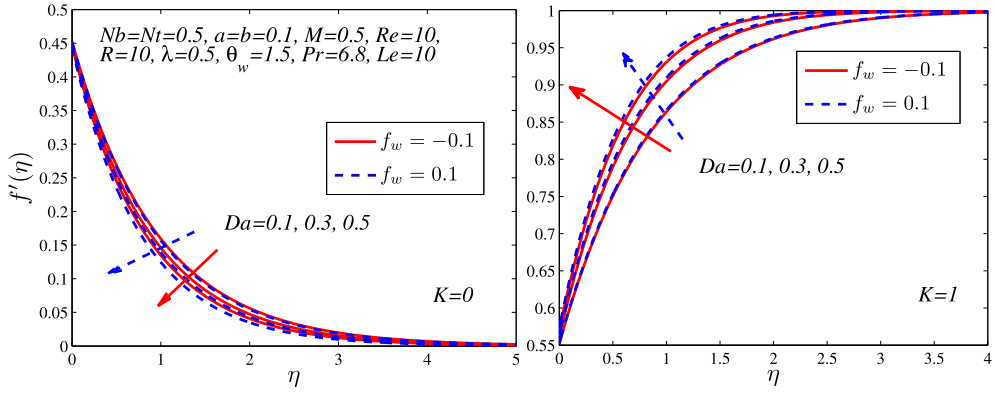

Figure 7 (a and b) Effect of Darcy number and suction/injection parameter on dimensionless velocity.

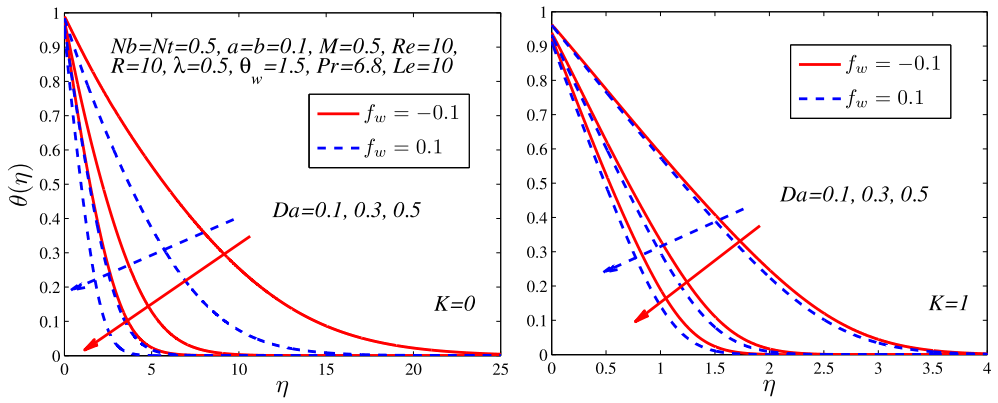

Figure 8 (a and b) Effect of Darcy number and suction/injection parameter on dimensionless temperature.

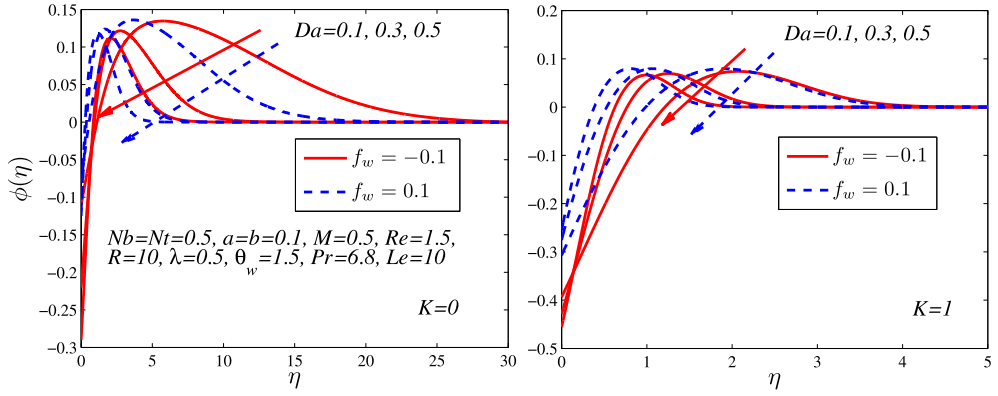

Figure 9 (a and b) Effect of Darcy number and suction/injection parameter on dimensionless concentration.

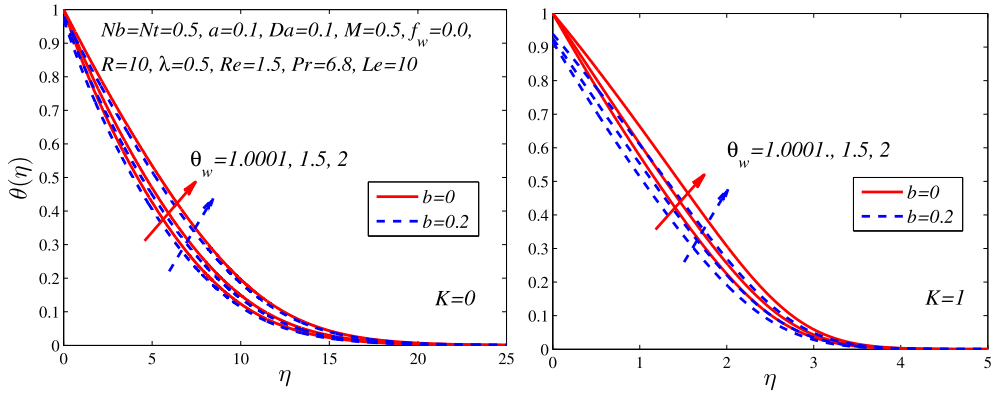

Figure 10 (a and b) Effect of thermal slip and temperature ratio on dimensionless temperature.

Fig. 11(a and b) presents the influence of temperature ratio and thermal slip parameters on the dimensionless nanoparticle volume fraction. Apparently the concentration of nanoparticles (as quantified by nanoparticle volume fraction) is elevated as the temperature ratio increases both in the absence and in the presence of the pressure gradient term and for both slip and non-slip conditions. For both pressure gradient cases, nanoparticle volume fraction is *initially* boosted but *subsequently* reduced as the thermal slip parameter increases. This effect is more prominent in the absence of pressure gradient. It is pertinent also to note that distinct from velocity and temperature distributions, which are always positive, irrespective of the parameter varied (even with strong wall suction), concentration magnitudes commence with negative values in all nanoparticle volume fraction plots. This phenomenon has been identified by other researchers e.g. Pera and Gebhart [59] and is hypothesized to be due to intense species transfer from the wall to the boundary layer at Lewis numbers exceeding unity (in our case $Le = 10$ is prescribed). Asymptotic convergence of all profiles is obtained in Figs. 2–11, confirming the specification of a sufficiently large infinity boundary condition in the finite element computations.

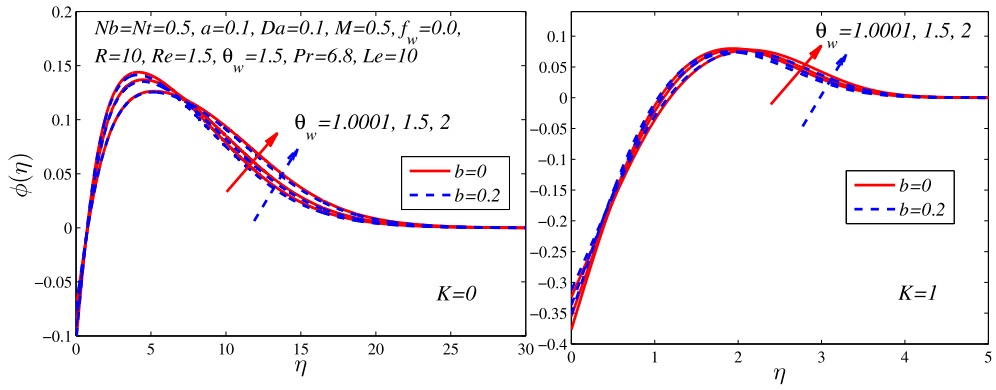

Figure 11 (a and b) Effect of thermal slip and temperature ratio on dimensionless concentration.

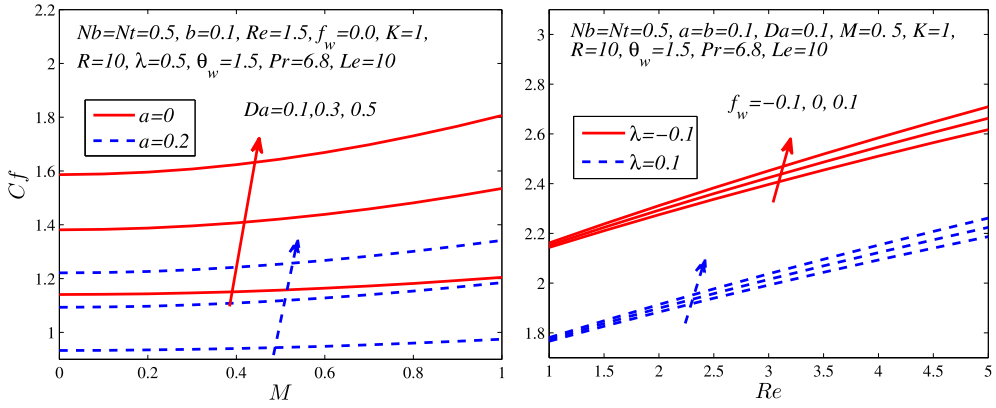

Figure 12 (a and b) Effect of the various parameters on the friction factor.

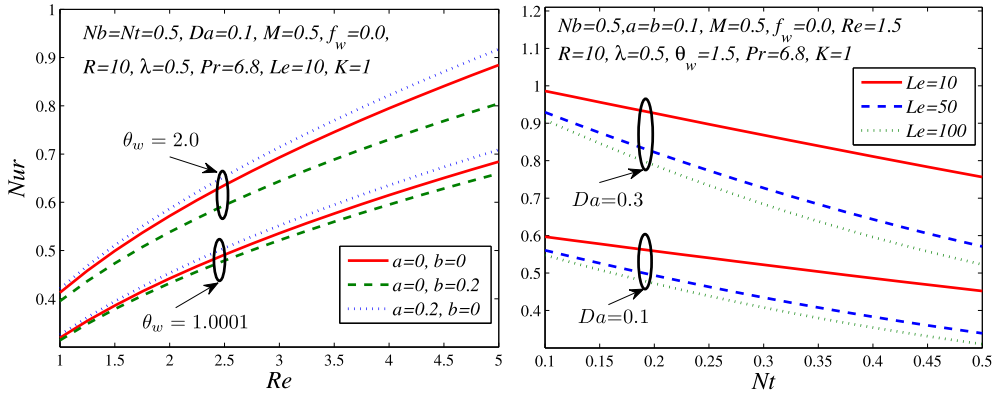

Figure 13 (a and b) Effect of the various parameters on the heat transfer rates.

Figs. 12–14 illustrate the effects of various parameters on the shear stress, the heat transfer rates, and mass transfer rates. Fig. 12(a and b) depicts the effects of the various parameters on the friction factor and indicates that friction increases as the Darcy number and the magnetic field parameter increase for both slip flow and no slip flow. The progressively weaker matrix resistance to nanofluid flow results in an acceleration which leads to greater shearing at the sheet surface and enhanced friction factor magnitudes. At first the influence of magnetic field appears to be at odds with the customary retarding behavior of Lorentz magnetohydrodynamic body force. However inspection of the momentum boundary layer equation reveals that the pressure gradient parameter alters the influence of magnetic field. Indeed this has been reported in a number of studies including Chamkha [60] and Anwar Bég [61], the former regarding Newtonian boundary layer magnetohydrodynamics and the latter addressing Newtonian, non-Newtonian and nanoscale flows. Momentum boundary layer

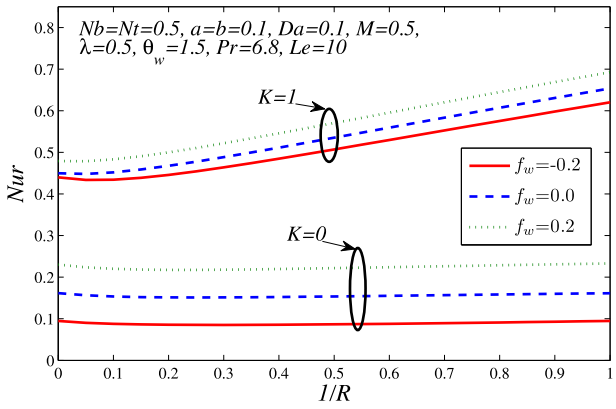

Figure 14 Effect of the various parameters on the heat transfer rates.

thickness is reduced with greater magnetic field. As expected, the slip velocity reduces the friction factor since the gradient of the velocity at the wall decreases. This is clearly observed from the boundary condition $f'(0) = \lambda + af''(0)$. As $a \to \infty$, the shear stress at the wall is almost zero. One can observe from Fig. 12(b) that friction increases with the Reynolds number for both the stretching sheet ($\lambda = 0.1$) and shrinking sheet ($\lambda = -0.1$) for both permeable and impermeable sheets. As expected, the injection enhances and suction decreases the friction factor. Fig. 13(a and b) shows the variation of the various parameters on the heat transfer rates. The heat transfer rates increases as the Reynolds number increases for both slip flow and no slip flow (Fig. 13(a)). Evidently a greater inertial effect in nanofluid flow exacerbates heat diffusion from the sheet to the fluid. Similar patterns have been documented by Dayyan et al. [47]. Temperature ratio is found to enhance the heat transfer rates for both slip and no slip flow (Fig. 13(a)). A similar result is also demonstrated by Hossain and Takhar [62]. It is found from Fig. 13(b) that heat transfer rate is decreased with the thermophoresis parameter (corresponding to a boost in temperatures in the boundary layer). Nanoscale thermophoresis therefore has a potent influence on heat transfer behavior at the sheet. Darcy number increases the heat transfer rates. However, Lewis number reduces the heat transfer rates. Finally, the variation of the inverse of the radiation parameter, suction/injection parameter and the pressure gradient parameter on the heat transfer rates is displayed in Fig. 14. The heat transfer rates increase as the inverse of the radiation parameter increases (corresponding to greater radiative flux contribution) in the presence of the pressure gradient for both permeable and impermeable sheet cases (Fig. 14(a)). No significant effect of the inverse of the radiation parameter on the heat transfer is found when there is no pressure gradient term. This feature has also been reported by Lord and Arpaci [51] albeit for Newtonian variable optical thickness boundary layer flows. Strong wall blowing (injection) depresses reduced Nusselt number values whereas strong suction results in the contrary behavior.

Fig. 15(a and b) depicts the influence of illustrating the effects of various parameters on the reduced Sherwood number (*Shr*) i.e. the wall mass transfer rate (nano-particle concentration gradient at the wall). In Fig. 15(a), *Shr* magnitudes are observed to be significantly elevated with increasing Reynolds number (*Re*). In other words an increase in inertial force relative to viscous force encourages species diffusion of nanoparticles to the wall from the boundary layer. Conversely increasing wall temperature excess ratio parameter $\left(\theta_w = \frac{T_w}{T_\infty}\right)$ is found to significantly depress *Shr* magnitudes. An increase in hydrodynamic slip (i.e. *a*) leads to a marked increase in *Shr* values whereas a rise in thermal slip parameter (i.e. *b*) *weakly* increases *Shr*. Therefore hydrodynamic slip exerts a more beneficial effect on nano-particle species diffusion from the boundary layer to the wall. In Fig. 15(b) increase in Darcy number (*Da*) is found to very substantially enhance wall nano-particle mass transfer rates (*Shr*) whereas with increasing thermophoretic parameter (*Nt*), there is a gradual decreases in *Shr* magnitudes although the effect is more pronounced at higher Darcy number. An increase in Lewis number significantly elevates the *Shr* magnitudes at any Darcy number.

5. Conclusions

In this article, a nonlinear mathematical model for steady-state two-dimensional viscous incompressible magnetohydrodynamic

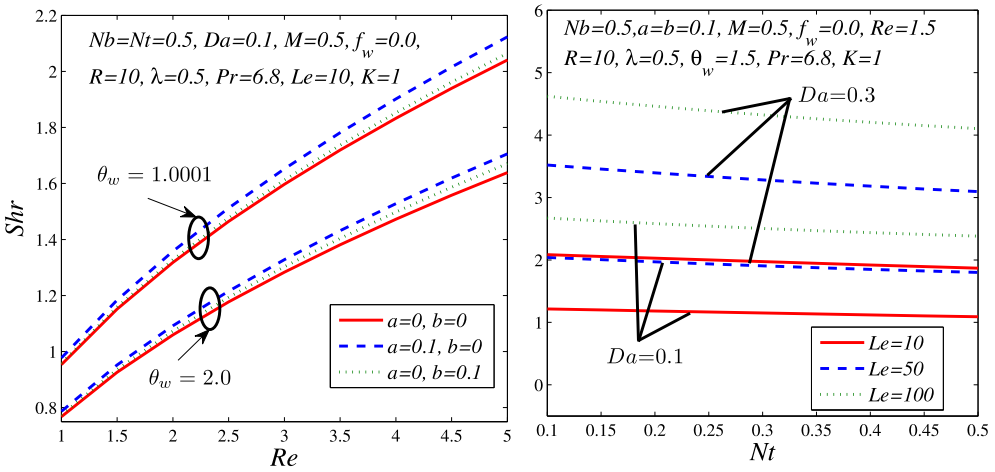

Figure 15 (a and b) Effect of the various parameters on the mass transfer rates.

slip flow of nanofluid from a nonlinearly radiating porous vertical extending/contracting sheet in a Darcian porous medium, has been developed. The study has been motivated by further investigating nano-material manufacturing processes based on the Sakiadis approach. The transport equations have been rendered into a system of non-dimensional ordinary differential equations using similarity transformations. A variational (weak form) finite element method (**FEM**) has been implemented to solve this boundary value problem numerically. Validation of the **FEM** results with earlier studies for regular fluids has been conducted, including mesh-independence. The main findings from the present computations may be summarized as follows:

(i) The surface friction factor increases as the Darcy number, the magnetic field parameter, and the Reynolds number increase.
(ii) Increasing velocity slip reduces the friction factor.
(iii) Heat transfer rates increase as the Reynolds number, the Darcy number and the temperature ratio are elevated.
(iv) Heat transfer rate is observed to be decreased with greater values of thermophoresis parameter and the Lewis number.
(v) Heat transfer rates increase as the inverse of the radiation parameter increases (i.e. as thermal radiative flux increases) in the presence of the pressure gradient for both permeable and impermeable sheet scenarios.
(vi) Nano-particle volume fraction (species concentration) is enhanced with larger temperature ratio both in the absence and in the presence of the pressure gradient term and also for both thermal slip and non-thermal slip cases.

Although the present work has been confined to the *steady-state* situation, future investigations will address *time-dependent* stretching/contracting sheet magnetic nanofluid flow and will explore other effects including Hall currents and more sophisticated radiative flux models.

Acknowledgments

The authors acknowledge financial support from Universiti Sains Malaysia, RU Grant 1001/PMATHS/811252. OAB would like to thank Emeritus Professor H.S. Takhar for some useful discussion in recent months regarding the physics of nanofluid boundary layers. Furthermore all the authors are grateful to the reviewers for their insightful comments which have served to enhance the clarity of the work.

References

[1] M.J. Uddin, W.A. Khan, A.I.M. Ismail, Free convection boundary layer flow from a heated upward facing horizontal flat plate embedded in a porous medium filled by a nanofluid with convective boundary condition, Transp. Porous Med. 92 (2012) 867–881.
[2] A. Aziz, W.A. Khan, I. Pop, Free convection boundary layer flow past a horizontal flat plate embedded in porous medium filled by nanofluid containing gyrotactic microorganisms, Int. J. Therm. Sci. 56 (2012) 48–57.
[3] S. Choi, Enhancing thermal conductivity of fluids with nanoparticle, in: Development and Applications of Non-Newtonian Flow, ASME Fluids Eng. Division, vol. 231/MD–vol. 66, 1995, pp. 99–105.
[4] M. Kole, T.K. Dey, Thermal conductivity and viscosity of Al_2O_3 nanofluid based on car engine coolant, J. Phys. D: Appl. Phys. 43 (2010) 315501.
[5] G.C. Bourantas, E.D. Skouras, V.C. Loukopoulos, V.N. Burganos, Heat transfer and natural convection of nanofluids in porous media, Eur. J. Mech. B/Fluids 43 (2014) 45–56.
[6] M. Kaviany, Principles of Heat Transfer in Porous Media, Springer-Verlag, NY, 1995.
[7] D.A. Nield, A. Bejan, Convection in Porous Media, third ed., Springer-Verlag, NY, 2013.
[8] K. Vafai, Handbook of Porous Media, Marcel Dekker, New York, 2000.
[9] P. Vadasz, Emerging Topics in Heat and Mass Transfer in Porous Media, Springer, New York, 2008.
[10] W. Yu, H. Xie, A review on nanofluids: preparation, stability mechanisms, and applications, J. Nanomater. 2012 (2012) 435873.
[11] J. Buongiorno, Convective transport in nanofluids, ASME J. Heat Transfer 128 (2006) 240–250.
[12] R.K. Tiwari, M.K. Das, Heat transfer augmentation in a two-sided lid-driven differentially heated square cavity utilizing nanofluids, Int. J. Heat Mass Transfer 50 (2007) 2002–2018.
[13] D.A. Nield, A.V. Kuznetsov, The Cheng-Minkowycz problem for natural convective boundary-layer flow in a porous medium saturated by a nanofluid, Int. J. Heat Mass Transfer 52 (2009) 5792–5795.
[14] A.J. Chamkha, R.S.R. Gorla, K. Ghodeswar, Non-similar solution for natural convective boundary layer flow over a sphere embedded in a porous medium saturated with a nanofluid, Transp. Porous Med. 86 (2011) 13–22.
[15] A. Noghrehabadi, A. Behseresht, Flow and heat transfer affected by variable properties of nanofluids in natural-convection over a vertical cone in porous media, Comput. Fluids 88 (2013) 313–325.
[16] A.M. Rashad, M.A. El-Hakiem, M.M.M. Abdou, Natural convection boundary layer of a non-Newtonian fluid about a permeable vertical cone embedded in a porous medium saturated with a nanofluid, Comput. Math. Appl. 62 (2011) 3140–3151.
[17] A. Mahdy, S.E. Ahmed, Laminar free convection over a vertical wavy surface embedded in a porous medium saturated with a nanofluid, Transp. Porous Med. 91 (2012) 423–435.
[18] C.Y. Cheng, Natural convection boundary layer flow over a truncated cone in a porous medium saturated by a nanofluid, Int. Commun. Heat Mass Transfer 39 (2012) 231–235.
[19] A. Behseresht, A. Noghrehabadia, M. Ghalambaz, Natural-convection heat and mass transfer from a vertical cone in porous media filled with nanofluids using the practical ranges of nanofluids thermo-physical properties, Chem. Eng. Res. Des. 9 (2) (2014) 447–452.
[20] D. Srinivasacharya, O. Surender, Non-similar solution for natural convective boundary layer flow of a nanofluid past a vertical plate embedded in a doubly stratified porous medium, Int. J. Heat Mass Transfer 71 (2014) 431–438.
[21] R.A. Mahdi, H.A. Mohammed, K.M. Munisamy, N.H. Saeid, Review of convection heat transfer and fluid flow in porous media with nanofluid, Renew. Sustain. Energy Rev. 41 (2015) 715–734.
[22] M. Behzad, V. Aliakbar, M. Shams, A. Moshfegh, Heat transfer analysis of a micro-spherical particle in the slip flow regime by considering variable properties, Heat Transfer Eng. 36 (2015) 596–610.
[23] F. Yang, Slip boundary condition for viscous flow over solid surfaces, Chem. Eng. Commun. 197 (2010) 544–550.
[24] Z. Wen-Ming, G. Meng, X. Wei, A review on slip models for gas microflows, Microfluid. Nanofluid. 13 (2012) 845–882.

[25] D. Tripathi, O. Anwar Bég, J. Curiel-Sosa, Homotopy semi-numerical simulation of peristaltic flow of generalized Oldroyd-B fluids with slip effects, Comput. Methods Biomech. Biomed. Eng. 17 (2014) 433–442.
[26] M.M. Nandeppanavar, K. Vajravelu, M. Subhas Abel, M.N. Siddalingappa, Second order slip flow and heat transfer over a stretching sheet with non-linear Navier boundary condition, Int. J. Therm. Sci. 58 (2012) 143–150.
[27] R. Bhargava, O. Anwar Bég, S. Vedad, M. Zeinalkhani, A. Heidari, Finite element analysis of multi-physical slip flow and heat transfer from a porous rotating disk, Int. J. Pure Appl. Sci. Technol. 11 (2012) 8–33.
[28] M.M. Khader, A.M. Megahed, Effect of viscous dissipation on the boundary layer flow and heat transfer past a permeable stretching surface embedded in a porous medium with a second-order slip using Chebyshev finite difference method, Transp. Porous Med. 105 (2014) 487–501.
[29] R.U. Haq, S. Nadeem, Z.H. Khan, N. Sher Akbar, Thermal radiation and slip effects on MHD stagnation point flow of nanofluid over a stretching sheet, Physica E 65 (2015) 17–23.
[30] R. Nikbakhti, A.B. Rahimi, Double-diffusive natural convection in a rectangular cavity with partially thermally active side walls, J. Taiwan Inst. Chem. Eng. 43 (2012) 535–541.
[31] R. Nikbakhti, A. Saberi, Natural convection heat and mass transfer in a rectangular porous cavity having partially thermally active walls, Int. J. Mech. Eng. Robot. Res. 5 (2016) 72–76.
[32] G.E. Karniadakis, A. Beskok, N. Aluru, Microflows and Nanoflows: Fundamentals and Simulation, Springer-Verlag, New York, USA, 2005.
[33] M.J. Uddin, O. Anwar Bég, A.I.M. Ismail, Mathematical modelling of radiative hydromagnetic thermosolutal nanofluid convection slip flow in saturated porous media, Math. Probl. Eng. (2014), http://dx.doi.org/10.1155/2014/179172, 11 p 179172.
[34] E.M. Sparrow, R.D. Cess, Radiation Heat Transfer, Hemisphere, Washington, 1978 (Chapters 7 & 10).
[35] O.D. Makinde, A. Aziz, Boundary layer flow of a nanofluid past a stretching sheet with a convective boundary condition, Int. J. Therm. Sci. 50 (2011) 1326–1332.
[36] A.V. Kuznetsov, D.A. Nield, Natural convective boundary-layer flow of a nanofluid past a vertical plate: a revised model, Int. J. Therm. Sci. 77 (2014) 126–129.
[37] S. Siddiq, M.A. Hossain, S.C. Saha, The effect of thermal radiation on the natural convection boundary layer flow over a wavy horizontal surface, Int. J. Therm. Sci. 84 (2014) 143–150.
[38] P. Rana, R. Bhargava, Flow and heat transfer over a nonlinearly stretching sheet: a numerical study, Commun. Nonlinear Sci. Numer. Simul. 17 (2012) 212–226.
[39] P. Rana, R. Bhargava, O. Anwar Bég, Finite element simulation of unsteady magneto-hydrodynamic transport phenomena on a stretching sheet in a rotating nanofluid, J. Nanoeng. Nanosyst. 227 (2013) 77–99.
[40] P. Rana, O. Anwar Bég, Mixed convection flow along an inclined permeable plate: effect of magnetic field, nanolayer conductivity and nanoparticle diameter, Appl. Nanosci. (2014), http://dx.doi.org/10.1007/s13204-014-0352-z.
[41] J.L. Curiel Sosa, O. Anwar Bég, J.M. Liebana Murillo, Finite element analysis of structural instability using a switching implicit–explicit technique, Int. J. Comput. Methods Eng. Sci. Mech. 14 (2013) 452–464.
[42] C.C. Chan, K.T. Chau, Design of electrical machines by the finite element method using distributed computing, Comput. Ind. 17 (1991) 367–374.
[43] L. Ren, Z. Qian, Finite element modeling in the musculoskeletal system: generic overview, Comput. Model. Biomech. Biotribol. Musculoskelet. Syst. (2014) 12–38.
[44] A. Cragges, A finite element model for acoustically-lined small rooms, J. Sound Vib. 108 (1986) 327–337.
[45] J.N. Reddy, An Introduction to Finite Element Method, third ed., McGraw-Hill, New York, 2005.
[46] K.A. Yih, The effect of uniform suction/blowing on heat transfer of magnetohydrodynamic Hiemenz flow through porous media, Acta Mech. 130 (1998) 147–158.
[47] M. Dayyan, S.M. Seyyedi, G.G. Domairry, M. Gorji Bandpy, Analytical solution of flow and heat transfer over a permeable stretching wall in a porous medium, Math. Probl. Eng. (2013), 10 p 682795.
[48] K. Suhil, M.A. Al-Nimr, Investigation into the similarity solution for boundary layer flows in microsystems, ASME J. Heat Transfer 132 (2010) 041011.
[49] A. Jawad, A. Oubarra, Hydrodynamic and thermal characteristics of laminar slip flow over a horizontal isothermal flat plate, ASME J. Heat Transfer 135 (2013) 021704.
[50] M.A. Hossain, M.A. Alim, D.A.S. Rees, The effect of radiation on free convection from a porous vertical plate, Int. J. Heat Mass Transfer 42 (1999) 181–191.
[51] H.A. Lord, V.S. Arpaci, Effect of non-gray thermal radiation on laminar forced convection over a heated horizontal plate, Int. J. Heat Mass Transfer 13 (1970) 1737–1751.
[52] H.A. Pakravan, M. Yaghoubi, Combined thermophoresis, Brownian motion and Dufour effects on natural convection of nanofluids, Int. J. Therm. Sci. 50 (2011) 394–402.
[53] F.M. Hady, F.S. Ibrahim, S.M. Abdel-Gaied, M.R. Eid, Radiation effect on viscous flow of a nanofluid and heat transfer over a nonlinearly stretching sheet, Nanoscale Res. Lett. 7 (2012) 229.
[54] M. Sheikholeslami, D.D. Ganji, M.Y. Javed, R. Ellahi, Effect of thermal radiation on magnetohydrodynamics nanofluid flow and heat transfer by means of two phase model, J. Magn. Magn. Mater. 374 (2015) 36–43.
[55] P.M. Adler, Porous Media – Geometry and Transports, Butterworths, USA, 1992.
[56] K. Vafai, C.L. Tien, Boundary and inertia effects on convective mass transfer in porous media, Int. J. Heat Mass Transfer 25 (1982) 1183–1190.
[57] K. Vafai, Convective flow and heat transfer in variable porosity media, J. Fluid Mech. 147 (1984) 233–259.
[58] B. Gebhart, Heat Conduction and Mass Diffusion, McGraw-Hill, New York, 1993.
[59] L. Pera, B. Gebhart, Natural convection flows adjacent to horizontal surfaces resulting from the combined buoyancy effects of thermal and mass diffusion, Int. J. Heat Mass Transfer 15 (1972) 269–278.
[60] A.J. Chamkha, Unsteady MHD convective heat and mass transfer past a semi-infinite vertical permeable moving plate with heat absorption, Int. J. Eng. Sci. 42 (2004) 217–230.
[61] O. Anwar Bég, Numerical methods for multi-physical magnetohydrodynamics, in: New Developments in Hydrodynamics Research , Nova Science, New York, September 2012, pp. 1–112 (Chapter 1).
[62] M.A. Hossain, H.S. Takhar, Radiation effect on mixed convection along a vertical plate with uniform surface temperature, Heat Mass Transfer 31 (1996) 243–248.
[63] W.A. Khan, I. Pop, Boundary-layer flow of a nanofluid past a stretching sheet, Int. J. Heat Mass Transfer 53 (2010) 2477–2483.

Please cite this article in press as: M.J. Uddin et al., Finite element simulation of magnetohydrodynamic convective nanofluid slip flow in porous media with nonlinear radiation, Alexandria Eng. J. (2016), http://dx.doi.org/10.1016/j.aej.2016.04.021